PHYSICAL SCIENCES

Strain propagation in layered two-dimensional halide perovskites

Jianhui Fu[1], Qiang Xu[1], Ibrahim Abdelwahab[2], Rui Cai[1], Benny Febriansyah[3], Tingting Yin[1], Kian Ping Loh[2], Nripan Mathews[4], Handong Sun[1], Tze Chien Sum[1]*

Impulsive light excitation presents a powerful tool for investigating the interdependent structural and electronic responses in layered two-dimensional (2D) halide perovskites. However, detailed understanding of the nonlinear lattice dynamics in these soft hybrid materials remains limited. Here, we explicate the intrinsic strain propagation mechanisms in 2D perovskite single crystals using transient reflection spectroscopy. Ultrafast photoexcitation leads to the generation of strain pulses via thermoelastic (TE) stress and deformation potential (DP) interaction whence their detection proceed via Brillouin scattering. Using a two-temperature model together with strain wave propagation, we discern the TE and DP contributions in strain generation. Hot carrier cooling plays a dominant role in effecting the weak modulation amplitude. Out-of-plane lattice stiffness is reduced by the weak van der Waals bond between organic layers, resulting in a slow strain propagation velocity. Our findings inject fresh insights into the basic strain properties of layered perovskites critical for manipulating their functional properties for new applications.

INTRODUCTION

Self-assembled 2D organic-inorganic lead halide perovskites (A_2PbX_4; where A is an organic cation and X is Br and I) are formed by a 2D connectivity of the corner-sharing PbX_6 octahedra sandwiched between bulky organic spacer bilayers with low refractive index and a large bandgap. The quantum confinement arising from their naturally formed multiple-quantum well structure and the dielectric confinement due to the considerable dielectric constant contrast between the organic barrier layer and the inorganic well layer give rise to fascinating properties, such as large exciton binding energies (*1*), strong exciton-phonon coupling (*2*, *3*), giant oscillator strength (*4*), and enhanced scintillation (*5*). These remarkable physical properties together with their facile fabrication and robust chemical stability propelled 2D halide perovskites' rise as forerunners in broad applications as solar cells (*6*), light-emitting diodes (*7*), photodetectors (*8*), and Seebeck generators (*9*). The soft nature of the halide perovskite lattice presents exciting opportunities to further manipulate their optoelectronic properties (*10*) and stability (*11*) through strain engineering. Notwithstanding, these soft materials are inevitably subjected to strain created at an interface during device fabrication or operation (e.g., mismatched thermal expansion coefficients), which could markedly influence optoelectronic properties and material stability (*12*). While modulation effects from static strain engineering have been well reported, ultrafast picosecond strain engineering, which affords a new paradigm to in situ monitoring of chemical reactions (*13*) and fast switching of optoelectronic (*14*, *15*) and magnetic properties (*16*), remains unexplored. Although ultrasonic strain–induced coherent longitudinal acoustic (LA) phonon scattering in 2D perovskites was recently reported, a clear understanding of the interrelated mechanisms of strain generation, propagation, and detection is still lacking (*17*, *18*). In particular, laser-induced ultrasonic strain propagation velocity v is determined by a single probe wavelength using $f = 2vn/\lambda$, where f, n, and λ are the oscillation frequency, refractive index, and probe wavelength, respectively (*18*–*20*). This simple equation could result in a different strain propagation velocity for a different probe wavelength (*21*), which is misleading from the physical point of view. Moreover, the strain generation mechanism in 2D halide perovskites is still under debate, with one study attributing to the dominant TE effect (*18*), while another ascribing to relative contributions from both the TE effect and DP interaction (*17*). Furthermore, it remains unclear how strain generation is affected by slow hot carrier cooling (HCC), a phenomenon that has been widely reported in halide perovskites. Previously, all studies assumed that the photoexcited carriers with excess energies instantaneously relax down to the band edge, generating the TE stress (*17*–*20*). However, this needs not be the case in the presence of slow HCC (*22*, *23*). Hence, addressing these open questions is not only of fundamental interest but also relevant for exploring ultrafast strain engineering as an approach to manipulate the functional properties of perovskites or to control collective excitations.

Here, we investigate the intrinsic picosecond strain propagation in 2D halide perovskite single crystals (SCs) using transient reflection (TR) spectroscopy. We seek to explicate the intrinsic interdependent mechanisms of strain generation, propagation, and detection in a model 2D perovskite system largely free from the effects of the substrate and multiple phases. Through detailed pump energy–dependent studies together with density functional theory (DFT) calculations, we establish that DP interaction also has a notable contribution to the strain generation. Using a two-temperature model together with strain wave propagation, we simulate the strain generation and detection processes. Our findings reveal that the reduced lattice rigidity due to the presence of the van der Waals (vdW) bond between organic spacers retards the strain propagation velocity. With a longer cooling time, HCC plays an important role in strain generation that leads to a gentler distribution of the

---

[1]Division of Physics and Applied Physics, School of Physical and Mathematical Sciences, Nanyang Technological University, 21 Nanyang Link, Singapore 637371, Singapore. [2]Department of Chemistry, National University of Singapore, 3 Science Drive 3, Singapore 117543, Singapore. [3]Energy Research Institute @NTU (ERI@N), Interdisciplinary Graduate School, Nanyang Technological University, 50 Nanyang Drive, Singapore 637553, Singapore. [4]School of Materials Science and Engineering, Nanyang Technological University, 50 Nanyang Avenue, Singapore 639798, Singapore.
*Corresponding author. Email: tzechien@ntu.edu.sg

out-of-plane lattice temperature and a resultant weaker strain modulation amplitude.

RESULTS

Strain generation, propagation, and detection by TR spectroscopy

We first examine these processes in the archetypal 2D halide perovskite, phenylethylammonium lead iodide [$(PEA)_2PbI_4$] SC flakes. Details on the SC preparation and basic properties are found in Materials and Methods and in figs. S1 to S3. All measurements were conducted at room temperature (RT) except when mentioned otherwise. X-ray diffraction (XRD) measurements (fig. S1) confirm that the layered PbI_6 octahedron network lies in-plane of the SC flake. The samples were photoexcited using above-bandgap femtosecond laser pulses, and strain propagation was probed using TR spectroscopy.

Figure 1A shows a schematic of the strain generation, propagation, and detection processes in the layered $(PEA)_2PbI_4$ SC sample. Above-bandgap pump pulse excitation generates an elastic strain pulse at the sample's surface that propagates into the bulk at the speed of sound v (*24*). The strain generation with ultrafast laser excitation is based on the conversion of pump photon energy into mechanical energy by the photoinduced stress (*24*). This propagating strain pulse modifies the local refractive index and reflects the penetrating probe light. The interference between the reflected probe light from the sample surface and that from the propagating strain pulse produces a periodic modulation of the optical reflectivity. This modulation amplitude depends on the strength of the photoinduced stress and, thus, the incident pump photon energy, whereas the oscillation period is governed by the probe wavelength, refractive index, and the speed of sound. Figure 1B shows a 2D contour plot of the TR spectrum of $(PEA)_2PbI_4$ SCs pumped at 400 nm with a fluence of 0.3 mJ cm^{-2}. The TR spectrum (e.g., at 5 ps of the red curve in Fig. 1B) generally shows a derivative profile with respect to the absorption change (*25*). This is due to the change in refractive index dominated by the state-filling effect, which depends on the photoexcited carrier concentration. To extract the strain-induced reflectance change, we subtract the carrier recombination and diffusion contribution using the multiple-exponential decay and obtain its residual. Typical TR decay kinetics probed at 542 nm, the curve fitting, and its residual are shown in Fig. 1C. As shown, the oscillation damps over nanosecond time scale.

Figure 1D shows the pump fluence–dependent oscillation kinetics probed at 542 nm. It is clear that the oscillation amplitude exhibits a linear dependence on pump fluence (inset of Fig. 1D), and the oscillation kinetics remain largely invariant except for their amplitudes when varying the pump photon energy (Fig. 1E). To examine the pump energy–dependent strain modulation dynamics, we fitted the oscillation kinetics using a damped oscillator function

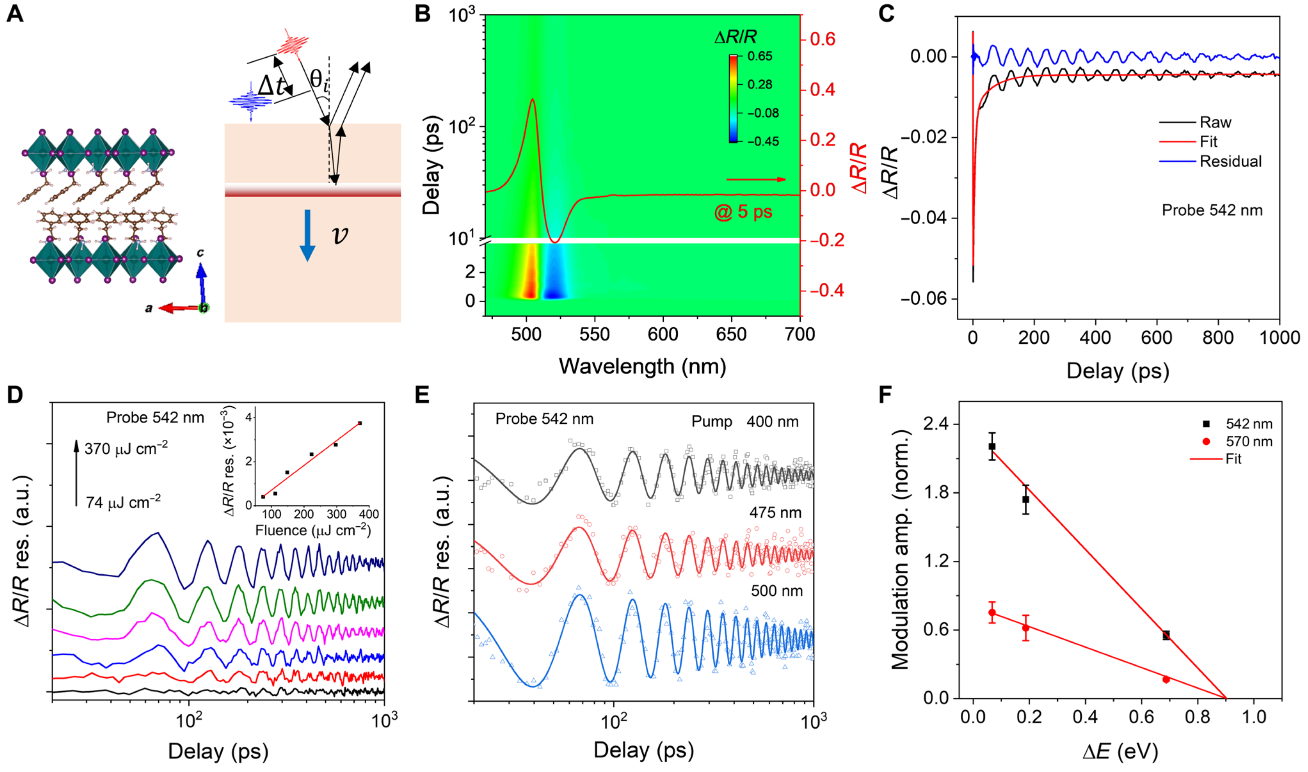

Fig. 1. Strain propagation and its modulation to the TR spectrum of $(PEA)_2PbI_4$ SCs. (**A**) Schematic of strain generation, propagation, and subsequent detection by TR spectroscopy in $(PEA)_2PbI_4$ SCs. (**B**) 2D contour plot showing the TR spectrum and a typical TR spectrum (red curve) at a delay of 5 ps of $(PEA)_2PbI_4$ SCs excited at 400 nm with a fluence of 0.3 mJ cm^{-2}. (**C**) Typical TR kinetics (black curve), curve fitting (red curve), and residual (blue curve) after subtracting contributions from carrier recombination and diffusion at a probe wavelength of 542 nm. (**D**) Pump fluence–dependent $\Delta R/R$ oscillation at 542 nm. Inset shows the $\Delta R/R$ oscillation amplitude as a function of pump fluence (black scatters) and the linear fit (red line). (**E**) Excitation energy–dependent $\Delta R/R$ oscillation probed at 542 nm. The colored curves are fittings using Eq. 1. (**F**) Normalized strain-induced modulation amplitude as a function of excess carrier energy for the two probes at 542 and 570 nm. The red lines are the global fits using Eq. 3. The error bars are from the curve fitting in (E). a.u., arbitrary units.

$$y = A e^{-t/\tau} \cos(2\pi f t + \phi) \qquad (1)$$

where A, τ, f, and ϕ are the oscillation amplitude, lifetime, frequency, and phase of the strain, respectively. Details of the fitting are shown in table S1. Given that the strain modulation amplitude is proportional to the initial photoexcited carrier density, we can therefore compare the normalized TR oscillation amplitude with respect to the carrier density to study how the strain-induced modulation amplitude varies with the excess energy (i.e., $\Delta E = E_0 - E_g$, where E_0 and E_g are the pump energy and optical bandgap, respectively) of the photoexcited carriers. The normalized oscillation amplitude with respect to the initial carrier density as a function of excess energy of photoexcited carriers for the probes at 542 and 570 nm is shown in Fig. 1F. It is obvious that, with increasing excess energy, the normalized oscillation amplitude decreases. This pump energy–dependent modulation amplitude is determined by the lattice generation process (see Eq. 3 below). Meanwhile, for the same pump, the normalized strain modulation with probe at 542 nm is much larger than that at 570 nm, which can be attributed to their different photoelastic constants in the strain detection process (see later discussion).

Lattice strain is present whenever there is lattice stress. Briefly, stress, which is a tensor, characterizes forces applied to the material system, whereas strain refers to the deformation under stress. This is especially important for soft materials that are not perfectly rigid; the constituents within move with respect to one another, and deformation results. There are mainly three contributions to the lattice stress after photoexcitation: (i) TE stress, (ii) DP interaction, and (iii) inverse piezoelectric interaction. The first (i) occurs when the photoexcited carriers transfer their excess energies to the lattice via electron-phonon interaction as they relax down to the band edge, generating a fast increase in lattice temperature, which yields the resultant TE stress (*24*, *26*), $\sigma_{TE} = -3B\beta N\frac{E_0 - E_g}{C_V}$, where B, β, N, and C_V are the bulk modulus, linear thermal expansion coefficient, carrier density, and volumetric heat capacity, respectively. The second (ii) occurs when the lattice equilibrium is broken and deformed by the change of electronic distribution after photoexcitation, which, in turn, modifies the band structure, inducing electronic stress (*24*), $\sigma_{DP} = -Nd$, where d is the sum of conduction band minimum (CBM) and valence band maximum (VBM) DP constants (details of DP definition can be seen in Materials and Methods) (*26*). Because excitons are the dominant photoexcited carrier species at thermal equilibrium because of their large exciton binding energy of ~0.2 eV (*27*), this parameter corresponds to the exciton DP. The last (iii) corresponds to screening of the intrinsic built-in electric field of a noncentrosymmetric material by the photoexcited charge carriers, which changes the equilibrium state of the lattice through the inverse piezoelectric effect, leading to the inverse piezoelectric stress, σ_{IP} (*26*, *28*). Considering that $(PEA)_2PbI_4$ is centrosymmetric and nonpiezoelectric with negligible built-in electric field (*29*, *30*), we discount this last contribution and only consider the TE and DP stress. The strain-induced TR coefficient r (which is related to the reflectivity or reflectance $R = |r|^2$) can be understood from Brillouin scattering, which gives rise to (*31*)

$$\frac{\Delta r}{r} = -2ik_0\delta z + \frac{2ik_0}{1-\tilde{n}^2}\int_0^{+\infty} \Delta\varepsilon \exp(2ik_0\tilde{n}z)\, dz \qquad (2)$$

In this equation, k_0 is the probe wave vector in air, $\tilde{n}$ is the complex refractive index, δz is the surface displacement, and $\Delta\varepsilon = 2(n + i\kappa)\left(\frac{\partial n}{\partial \eta} + i\frac{\partial \kappa}{\partial \eta}\right)\eta$ is the change in dielectric constant by the lattice strain $\eta = \frac{\partial u}{\partial z}$, where u is the lattice displacement. Note that the first and second terms on the right side of Eq. 2 correspond to phase modulation from the front side of the sample and the bulk photoelastic effect, respectively. The detected transient reflectance is then obtained as $\frac{\Delta R}{R} \approx 2\Re\left(\frac{\Delta r}{r}\right)$. Because the strain amplitude is proportional to photoexcited carrier density, it is expected that the strain-induced TR oscillation amplitude shows a linear dependence on pump fluence, which gives rise to

$$\left(\frac{\Delta R}{R}\right)_{osc} \propto \sigma = \sigma_{TE} + \sigma_{DP} = -3B\beta N\frac{E_0 - E_g}{C_V} - Nd \qquad (3)$$

Considering that the photoelastic effect varies for different probe wavelengths, to minimize fitting errors, we set d as a global parameter and perform global fitting to the normalized oscillation amplitude as a function of excess energy of photoexcited carriers using Eq. 3 for two probe wavelengths (fig. S4), as shown in Fig. 1F. With $B = 10.25$ GPa (*32*), $C_V = 1.19\ \mathrm{J\ K^{-1}\ cm^{-3}}$ (*33*), and $\beta = 1.8 \times 10^{-4}\ \mathrm{K^{-1}}$ (fig. S5 and note S1), we obtained the DP constant $d = -(4.3 \pm 0.2)$ eV, which agrees well with our calculated out-of-plane DP constant of −3.87 eV using DFT calculations. The non-negligible contribution from DP interaction can be further corroborated from TR measurements under near-resonant pump when the TE stress is zero (fig. S6). The negative DP constant, which means an increase in energy when the lattice contracts, is partly due to the kinetic energy effect and is also due to the strong antibonding character of the band-edge density of states (DOSs) (*34*, *35*). The calculated DP of the VBM ($d_h = -2.60$ eV) is twice that of the CBM ($d_e = -1.29$ eV), suggesting that the VBM is more susceptible to volume deformation than the CBM. We note that the DOS of VBM in $(PEA)_2PbI_4$ mainly consists of stronger Pb 6s and I 5p antibonding state compared to that of the CBM, which is dominated by antibonding Pb 6p and I 5p orbital state (*36*). This stronger antibonding character of the VBM compared to that of the CBM leads to a larger increase in energy when the lattice is contracted (*34*). The estimated DP of $(PEA)_2PbI_4$ is comparable to that of its 3D counterpart methylammonium lead iodide ($MAPbI_3$) (*19*) and is much smaller than that of GaAs (*26*). Details of our calculations are shown in Materials and Methods.

Strain-induced beating map and strain propagation simulation

Figure 2A shows the full beating map of strain modulation in the TR oscillation kinetics. As shown, the oscillation exhibits a strong dependence on probe wavelength, with its amplitude being the smallest at around the bandgap, and gradually decreases with increasing probe wavelength for below-bandgap regions. On the other hand, the oscillations of above-bandgap probe damp much faster than those for below-bandgap probes. This is because of considerable light absorption in the former, whereas damping is mainly due to phonon scattering by phonons, defects, or grain boundaries for the latter (demonstrated later). The oscillation period is longer for larger probe wavelength, which is a signature of strain propagation detection based on Brillouin scattering (*24*). Apart from the beating map contributed by the propagating strain, we also observed a beating map appearing in the first 10 ps (fig. S7). This beating map is due to phonon modulation of electronic states because of exciton-optical phonon coupling via DP interaction (*2*). To extract the modulation frequency caused by strain propagation, we performed a fast Fourier transform (FFT) of the beating map and fitted the FFT spectrum (fig. S8). Figure 2B shows

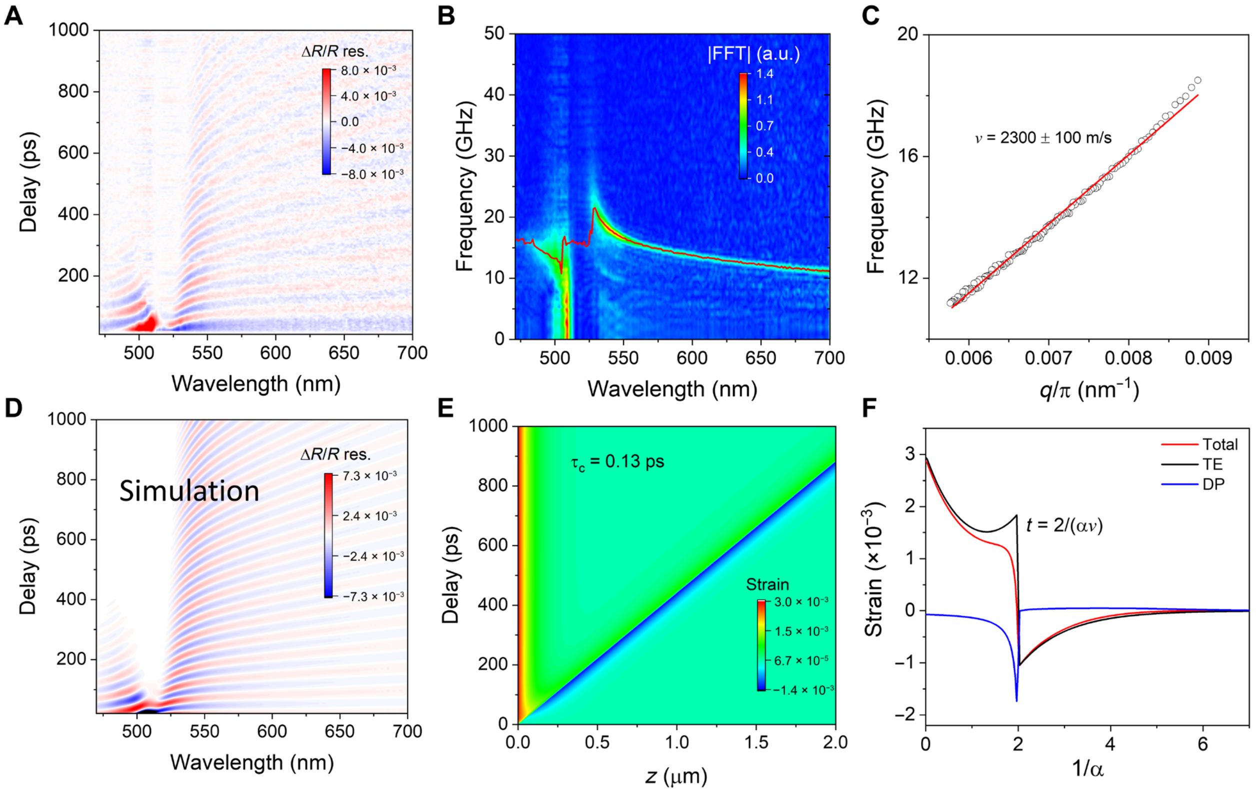

Fig. 2. Strain-induced beating map and the simulated strain. (**A**) 2D contour plot of the time-domain beating map of TR oscillation kinetics induced by strain propagation in $(PEA)_2PbI_4$ SCs. (**B**) Frequency domain of the beating map. The red curve is the probe wavelength–dependent strain modulation frequency. (**C**) Oscillation frequency as a function of probe light wave vector $q = 2\pi\sqrt{n^2 - \sin^2\theta_i}/\lambda$. (**D**) Simulated time-domain beating map in $(PEA)_2PbI_4$ SCs with a 400-nm pump at a fluence of 0.3 mJ cm^{-2} and HCC time τ_c of 0.13 ps. (**E**) Simulated strain propagation in $(PEA)_2PbI_4$ SCs. (**F**) Simulated strain contributed by TE stress (black curve), DP interaction (blue curve), and the sum (red curve) as a function of pump penetration depth at $t = \frac{2}{\alpha v}$.

that the oscillation frequency decreases with probe wavelength for both below- and above-bandgap regions. The FFT amplitude also shows a strong dependence on the probe wavelength, i.e., it first increases and then decreases with increasing probe wavelength (fig. S8). This probe wavelength dependence is governed by the strain detection process, which can be well explained by Brillouin scattering, i.e., interference of reflected light from the propagating lattice strain and the front surface of the sample (fig. S8 and note S2). Next, we estimate the strain propagation velocity on the basis of the strain detection process within the framework of Brillouin scattering. With the measured refractive index (fig. S3) and a probe incidence angle θ_i of 13°, we obtained the extracted strain propagation frequency as a function of the probe wave vector $q = \frac{2\pi\sqrt{n^2 - \sin^2\theta_i}}{\lambda}$ in the sample, where λ is the probe wavelength. From the linear fit (Fig. 2C), we obtained the strain propagation velocity $v = 2300 \pm 100$ m/s, which is consistent with the literature (*17*).

With this information, we detail the mechanism on how strain propagates in $(PEA)_2PbI_4$ SCs and compare our experimental results with simulations. For above-bandgap photoexcitation, the source of strain consists of TE stress and DP interaction. Here, we start from the strain generation process in $(PEA)_2PbI_4$ after 400 nm of photoexcitation with a pump fluence of 0.3 mJ cm^{-2} and assume that HCs lose their excess energies to the lattice and form excitons with an effective lifetime τ_c. This HCC will lead to an increase in lattice temperature associated with heat diffusion. Given the large exciton binding energy (~0.2 meV) (*27*), excitons cannot be directly generated with a 3.1-eV (or 400-nm) pump because of energy and momentum conservations (fig. S9). Here, we can describe the evolution of HC and lattice temperatures (i.e., T_c and T_L) using a simple two-temperature model, which yields the following differential equations

$$\frac{dT_c}{dt} = -\frac{T_c}{\tau_c} \tag{4}$$

$$C_V\frac{\partial T_L}{\partial t} = N\frac{3k_B}{2}\frac{T_c}{\tau_c} + \frac{\partial}{\partial z}k\frac{\partial T_L}{\partial z} \tag{5}$$

$$\frac{\partial N}{\partial t} = D\frac{\partial^2 N}{\partial z^2} - k_1 N - k_2 N^2 \tag{6}$$

where k, D, k_1, and k_2 are the thermal conductivity, carrier diffusion coefficient, and monomolecular and Auger recombination coefficients of the exciton, respectively. The initial and boundary conditions of Eqs. 4 to 6 are shown in note S3. The HCC time is estimated to be 0.13 ps and hardly depends on pump fluence (fig. S9). This is likely due to the strong Fröhlich interaction arising from the reduced Coulomb screening effect (i.e., low dielectric permittivity of the organic spacers) (*37*).

The spatially distributed exciton population $N(z, t)$ is modeled using a 1D carrier diffusion model, as described by Eq. 6. To simplify the HCC process, we have also disregarded the phonon scattering process [i.e., longitudinal optical (LO) phonon decays into acoustic phonons] in Eq. 5 and assumed that HCs relax and heat up the lattice directly because cooling is much faster in 2D halide perovskites than in their 3D counterparts (see Discussion later). To estimate D, k_1, and k_2, we conducted pump fluence–dependent TR measurements and obtained $D = 0.46 \pm 0.12\ \text{cm}^2\ \text{s}^{-1}$, $k_1 = (3.0 \pm 0.4) \times 10^8\ \text{s}^{-1}$, and $k_2 = (9.7 \pm 0.4) \times 10^{-9}\ \text{cm}^3\ \text{s}^{-1}$ (fig. S10 and note S3). The 1D lattice strain wave equation is then simulated according to (*24*) and (*38*) (note S4)

$$\rho \frac{\partial^2 u}{\partial t^2} = \frac{\partial \sigma}{\partial z} \tag{7}$$

where the stress σ is given by

$$\sigma = \rho v^2 \eta + \sigma_{\text{TE}} + \sigma_{\text{DP}} \tag{8}$$

Here, ρ is the mass density. With the initial condition $u(z,0) = u_0$ and boundary conditions $\sigma(z,0) = 0$ and $\sigma(L,0) = 0$, where u_0 is the initial lattice displacement, we can simulate the strain propagation and the induced oscillation in transient reflectance. Figure 2 (D and E) shows the 2D contour plot of strain-modulated TR spectrum and the corresponding strain propagation in $(\text{PEA})_2\text{PbI}_4$ SCs, respectively. Our simulated spectrum matches well with the experimental results for both below- and above-bandgap regions (Fig. 2A), consistent with Brillouin scattering in the strain detection process. The lattice strain is strongest at the sample's surface and propagates into the bulk sample at the speed of sound. As expected, the TE stress contribution to the lattice strain cancels that from DP interaction (Fig. 2F). The strain pulse consists of a region of expansion (or positive strain) followed by a region of compression (negative strain), in good agreement with previous results (*24*, *26*). Meanwhile, compared to heat and carrier diffusions (fig. S11), lattice strain propagates much faster, indicating that the lattice strain propagation is barely affected by carrier and heat diffusions. This can be verified from the negligible difference between the calculated strain in the presence and absence of heat and carrier diffusions (figs. S12 and S13).

Strain is also generated when large polarons are formed after photoexcitation because of the Fröhlich interaction (*39*). This generated strain due to the exciton-polaron formation is likely to only influence the background of the TR kinetics, as shown in a recent work (*39*). Even taking carrier diffusion into consideration, its effect on propagation strain is much weaker given that carrier diffusion is much slower compared with acoustic strain wave propagation, as mentioned previously. Nonetheless, this polaron effect is beyond the scope of our work. Similar background effects include defect-related strain generation and residual strain from the sample crystallization process. Again, this will not change our conclusion of laser-induced picosecond acoustic strain propagation. On the other hand, in Eqs. 3 and 5 and estimating the DP constant, we have ignored the Auger heating contribution, which only plays a negligible role in strain generation. This is because most of the HCs' excess energies are lost through the dominant Fröhlich interaction that occurs over a subpicosecond time scale. This has been demonstrated previously in perovskite bulk films (>99%) (*22*) and weakly confined nanocrystals (>94%) (*40*). Therefore, even for near-resonant photoexcitation, the effect of Auger heating on strain generation via the TE process is still negligible compared to DP interaction.

Strain propagation velocity decreased by vdW interaction

Next, we examine the influence of the organic linker (aromatic versus aliphatic) on the strain propagation properties in Ruddlesden-Popper (RP) and Dion-Jacobson (DJ) perovskite systems. Beginning with the aromatic systems, the two layers of organic cations (PEA^+) in $(\text{PEA})_2\text{PbI}_4$ RP perovskite are tethered to their adjacent PbI_6 layer by hydrogen bonding, respectively. In turn, these PEA^+ layers are held together by vdW interactions. In the $(\text{4AMP})\text{PbI}_4$ [4-(aminomethyl) piperidinium (4AMP)] DJ perovskite, the adjacent octahedral PbI_6 layers are connected by a single layer of organic cation 4AMP^{2+} via hydrogen bonding. XRD measurements establish that the *a* axis is along the out-of-plane direction of the DJ SCs (fig. S14).

Through similar transient reflectivity measurements for the $(\text{4AMP})\text{PbI}_4$ SC flakes, we obtain its propagation velocity $v = 2450 \pm 80$ m/s (fig. S14), which is higher than that of $(\text{PEA})_2\text{PbI}_4$ (Fig. 3A). Treating the PbI_6 octahedron and organic spacer as two distinct masses in a linear biatomic lattice (Fig. 3B), we model the RP perovskites using a bead-spring model (or coupled oscillators). Figure 3C shows the calculated propagation velocity as a function of the spring constant k_a between the organic and inorganic lattice. Table 1 shows that the k_a value for $(\text{4AMP})\text{PbI}_4$ (i.e., 19.5 N/m) is more than twice that of $(\text{PEA})_2\text{PbI}_4$ (i.e., 7.6 N/m). This suggests that vdW bonding strongly reduces the effective spring constant and, thus, the lattice stiffness. To further assess the vdW bond strength, we construct a linear triatomic bead-spring model (Fig. 3D) and assume that the hydrogen bonding between the organic spacer and the inorganic lattice (*41*) is the same for $(\text{PEA})_2\text{PbI}_4$ RP and $(\text{4AMP})\text{PbI}_4$ DJ perovskites. Figure 3E shows the calculated strain propagation velocity as a function of the unit cell length l and the spring force constant of k_b between organic layers (see also fig. S15 and note S5). We obtain $k_b = 6.2$ N/m that is much smaller than the spring constant $k_a = 19.5$ N/m for hydrogen bonding (Table 1), in agreement with their expected bond strengths (i.e., hydrogen bond > vdW bond).

Extending to RP and DJ perovskites with aliphatic organic linkers, we obtained the propagation velocities for vdW-bonded *n*-butylammonium lead iodide [$(\text{BA})_2\text{PbI}_4$] RP system (fig. S16) and the butane-1,4-diammonium lead iodide [$(\text{BdA})\text{PbI}_4$] DJ system (fig. S17). vdW bonding present in $(\text{BA})_2\text{PbI}_4$ RP perovskite drastically decreases the effective spring constant, leading to a much slower propagation velocity of 1500 ± 400 m/s compared to 2110 ± 20 m/s in $(\text{BdA})\text{PbI}_4$ DJ perovskite (Table 1 and fig. S17). On the other hand, comparing the aromatic linker in $(\text{PEA})_2\text{PbI}_4$ and the aliphatic linker in $(\text{BA})_2\text{PbI}_4$, both the propagation velocity and spring constants of the latter are much smaller, indicating reduced lattice rigidity (Table 1 and fig. S16). This is attributed to the strong dipole-dipole and π-π interactions between the aromatic functional groups in $(\text{PEA})_2\text{PbI}_4$ that are absent in $(\text{BA})_2\text{PbI}_4$. This also suggests that the organic cation has a large influence on the vdW bond strength. The reduced lattice stiffness by the presence of vdW bonding can be further verified from the calculated Young's modulus $Y_{33} = \rho v^2$, where ρ is the mass density. From Fig. 3A, the Young's modulus of $(\text{PEA})_2\text{PbI}_4$ and $(\text{BA})_2\text{PbI}_4$ RP perovskites is 13.1 and 6.3 GPa, respectively, which are comparable to that of soft materials such as polymers or organic solids (Y_{33} of ~10 GPa) (*42*). Comparatively, the Young's modulus of $(\text{4AMP})\text{PbI}_4$ and $(\text{BdA})\text{PbI}_4$ DJ perovskites is much larger. Note that the estimated Young's modulus of $(\text{PEA})_2\text{PbI}_4$ is even smaller than that of typical transition metal dichalcogenides, such as MoS_2 (Y_{33} of ~32 to 60 GPa) (*43*). This agrees with its soft lattice nature

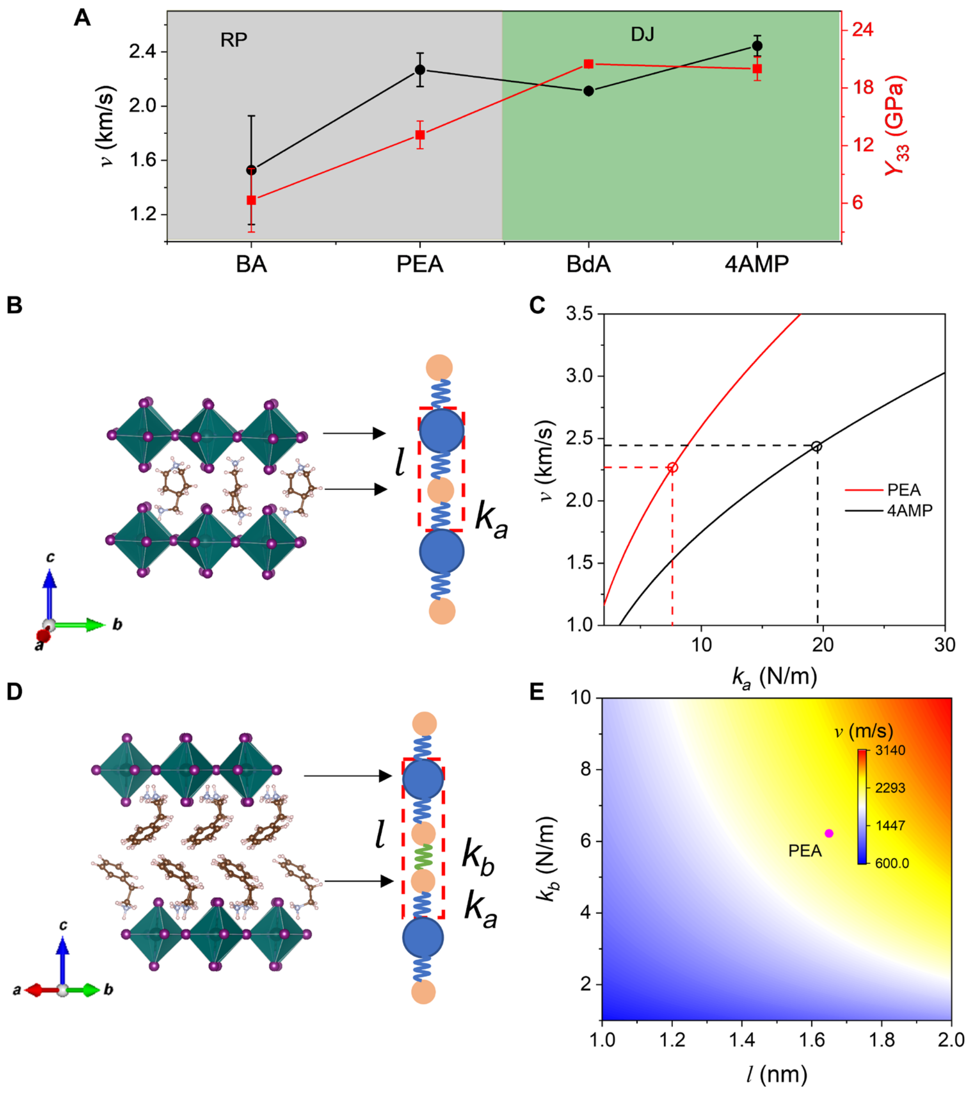

Fig. 3. Reduction of strain propagation velocity by vdW interaction. (**A**) Organic cation–dependent strain propagation velocity and Young's modulus of layered 2D perovskites. (**B**) Schematic crystal structure of $(4AMP)PbI_4$ and linear biatomic bead-spring model. Here, the blue sphere represents PbI_6 octahedron, while the beige sphere represents 4AMP and $(PEA)_2$, in $(4AMP)PbI_4$ and $(PEA)_2PbI_4$, respectively. (**C**) Calculated strain propagation velocity as a function of the spring constant k_a of a linear biatomic lattice chain. (**D**) Schematic crystal structure of $(PEA)_2PbI_4$ and linear triatomic lattice in which the blue and beige spheres represent PbI_6 octahedron and PEA, respectively. (**E**) Calculated strain propagation velocity as a function of the spring constant of k_b and the unit cell length l of a linear triatomic lattice.

because of the intrinsic soft organic sublattice and anharmonic inorganic PbX_6 octahedron (*44*).

DISCUSSION

To provide further insights into the strain propagation, we simulate the fluence-dependent strain propagation and its modulation to $\Delta R/R$ spectrum in $(PEA)_2PbI_4$ under a 400-nm pump with an HCC time τ_c of 0.13 ps. As expected, the strain (Fig. 4A) and its induced modulation amplitude (Fig. 4B) increase with pump fluence. Meanwhile, the induced $\Delta R/R$ oscillation occurs earlier when increasing the pump fluence (red dashed arrow). To explain this shift, we simulate the respective strain-induced modulation by TE stress and DP interaction (fig. S18). The slight shift with fluence is only observed under DP interaction, whereas it is barely discernible under TE stress, clarifying the origin. We note that there is a nonlinear Auger recombination term in Eq. 6. This contribution from nonradiative Auger recombination to carrier depopulation increases with increasing pump fluence, which brings about a faster onset of the oscillations, bearing in mind that strain due to DP interaction $\eta_{DP} = \frac{\partial \sigma_{DP}}{\partial z} \propto -\frac{\partial N}{\partial z}$ (fig. S18).

Next, we examine how strain and its modulation are affected by the HCC effect. Although HCC and exciton formation time is very fast and insensitive to pump fluence (fig. S9) (*37*), the time scale of this process varies with different organic cations, such as in ethylammonium lead iodide $[(EA)_2PbI_4]$ (*17*). Figure 4C shows that the strain is almost unchanged when $\tau_c \leq 1$ ps but decreases drastically when τ_c further increases. This is expected given that a shorter τ_c means a faster transfer of the excess energies of the photoexcited carriers to the lattice. Thus, the strain wave equation (Eq. 7) is solely governed

Table 1. Comparison of strain propagation velocities and derived spring constants using linear biatomic and triatomic lattice models between RP and DJ 2D layered perovskites.

Materials		**RP perovskites**		**DJ perovskites**	
		$(PEA)_2PbI_4$	**$(BA)_2PbI_4$**	**$(4AMP)PbI_4$**	**$(BdA)PbI_4$**
v (m/s)		2300 ± 100	1500 ± 400	2450 ± 80	2110 ± 20
Biatomic model	k_a (N/m)	7.6	4.6	19.5	14.6
Triatomic model	k_a (N/m)	19.5	14.6	–	–
	k_b (N/m)	6.2	3.3	–	–

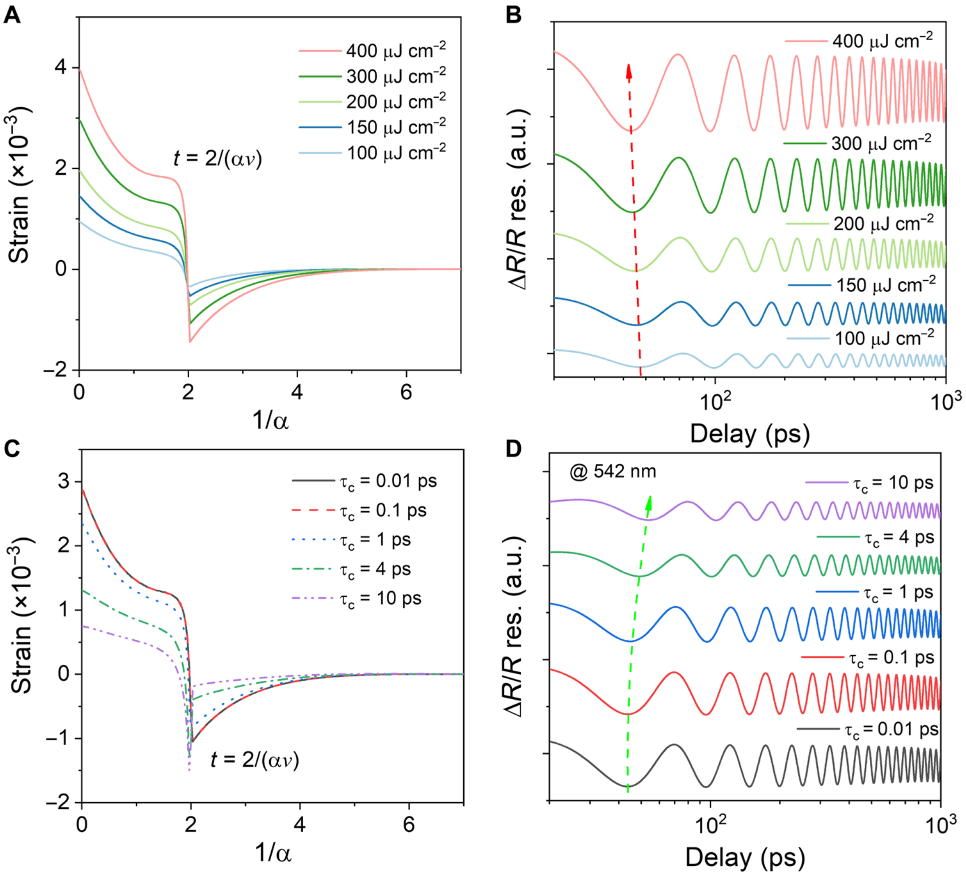

Fig. 4. Influence of HCC lifetime on strain generation and detection. Simulated pump fluence–dependent lattice strain in $(PEA)_2PbI_4$ at $t = \frac{2}{\alpha v}$ as a function of pump penetration depth (**A**) and the induced $\Delta R/R$ oscillation (**B**) probed at 542 nm for $\tau_c = 0.13$ ps. The red dashed arrow in (B) is a guide to the eye, illustrating that the $\Delta R/R$ oscillations occur earlier with increasing pump fluence. Simulated lattice strain (**C**) as a function of pump penetration depth at $t = \frac{2}{\alpha v}$ and the induced $\Delta R/R$ oscillation probed at 542 nm (**D**) for a different τ_c. The green dashed arrow in (D) is a guide to the eye, illustrating the delayed onset of the $\Delta R/R$ oscillations with increasing τ_c.

by other processes (i.e., heat diffusion, carrier recombination, and diffusion). The reduced strain amplitude with the growth of τ_c can be ascribed to a more moderate spatial distribution of lattice temperature given that the DP contribution remains unchanged. As a result, this reduced strain amplitude leads to a reduction of the modulation amplitude (Fig. 4D). This suggests that while 2D perovskite-based solar cells are more chemically stable, they may be suffering from intrinsic instability induced by strong lattice strain from heat inevitably generated during HCC under concentrated solar irradiation. On the other hand, the delayed HCC slows down the generation of TE stress, resulting in delayed strain modulation to the TR spectrum (green dashed arrow).

With our model, we successfully differentiated the contributions from TE stress and DP interaction to strain propagation and the resultant strain modulation on the optical properties in layered 2D perovskites. Although a rigorous treatment would invoke the three-temperature model consisting of HCs, LO phonons, and lattice (*45*), the ultrafast phonon scattering process ($\tau_{LO} < 1$ ps) in 2D halide perovskites has minimal effect on the strain generation and the resultant $\Delta R/R$ modulation. Thus, the two-temperature model would suffice here (figs. S19 and S20 and note S3). Our study of acoustic strain propagation velocity will be important for thermal management of the 2D perovskite-based devices, considering that the sound velocity is a key parameter of thermal conductivity. Meanwhile, the thermal conductivity of a semiconductor is generally dominated by LA phonon scattering with transverse acoustic phonon and optical phonon having negligible contributions because of their much lower group velocities. Within a generic kinetic theory, thermal conductivity k can be approximated as $\frac{1}{3}C_v v^2 \tau_0$, where τ_0 is the LA phonon lifetime because of phonon scattering by grain boundaries, defects, and phonon anharmonicity due to the three-phonon Umklapp process (*46*). For these high-purity SCs, phonon scattering is dominated by its intrinsic anharmonicity. Although the estimated LA phonon velocity and the reported C_v of $(PEA)_2PbI_4$ are comparable to those of its 3D counterpart $MAPbI_3$ (*19*, *21*), its cross-plane thermal conductivity is found to be less than half of the latter (*33*), which means that $(PEA)_2PbI_4$ has a shorter acoustic phonon lifetime. This suggests that phonon anharmonicity plays an important role in the ultralow thermal conductivity of $(PEA)_2PbI_4$. The shorter acoustic phonon lifetime of $(PEA)_2PbI_4$ may be attributed to additional vibrational scattering at the organic/organic interface between organic spacers connected by the weak vdW bond, as compared to the cluster rattling mechanism of organic molecules to the inorganic lattice that governs the acoustic phonon scattering in 3D perovskite (*47*). On the other hand, our results demonstrate that the presence of vdW bond, in which its strength is affected by the type of organic cation, also leads to a decrease in phonon velocity caused by reduced lattice rigidity. Together, these two factors result in the ultralow thermal conductivity of 2D halide perovskites.

In summary, we investigate the strain propagation process in layered 2D halide perovskites using ultrafast TR spectroscopy and theoretical modeling. We identify the mechanisms of strain generation and detection processes via detailed pump and probe energy–dependent modulation studies. Using a two-temperature model together with a 1D wave equation, we successfully reproduce the strain propagation and the resultant strain modulation on the TR spectrum. Meanwhile, we show that HCC plays an important role in strain generation, which affects both the phase and amplitude of the induced modulation. Nevertheless, compared to their 3D $MAPbI_3$ counterpart, HCC is much faster in 2D halide perovskites due to a stronger Fröhlich interaction. Furthermore, on the basis of the bead-spring model, we find that the interaction between organic spacers has a large effect on the strain propagation velocity in layered 2D halide perovskites. Our study injects fresh insights into strain propagation and the resultant strain modulation on the optical and electronic properties of 2D halide perovskites, which could unlock new opportunities for engineering their functional properties.

MATERIALS AND METHODS

Sample preparation

$(C_6H_5C_2H_4NH_3)_2PbI_4$ [or $(PEA)_2PbI_4$] and $(C_4H_9NH_3)_2PbI_4$ [or $(BA)_2PbI_4$] SC flakes were prepared using a modified temperature-cooling method according to (*48*). PEAI or BAI (Dyesol) and PbO (99%; trace metals basis, Acros Organics) with a stoichiometric molar ratio of 1:1 were dissolved in a mixture of hydroiodic acid and phosphoric acid with a concentration of 0.59 M. The obtained solution was then heated to boiling under constant magnetic stirring for about 5 min, which formed a bright yellow solution. Subsequently, the stirring was stopped, and the solution was cooled down to RT at a rate of 2°C/min, which formed orange crystals. The obtained crystals were then isolated with vacuum filtration thoroughly dried under reduced pressure. $(C_6H_{16}N_2)PbI_4$ [or $(4AMP)PbI_4$] SC flakes were grown according to (*49*). For the growth of $(C_4H_{14}N_2)PbI_4$ [or $(BdA)PbI_4$] SC flakes, BdAI source was first synthesized. Concentrated hydroiodic acid [aq., 57 weight % (wt %)] and hypophosphorus acid solution (aq.; Sigma-Aldrich) with a stoichiometric volume ratio of 1:0.025 were added to a mixture of ethanol and butane-1,4-diamine (99%; Sigma-Aldrich). After stirring the solution for 1 hour, the volatiles were removed using a rotary evaporator. The BdAI source was then obtained by washing the remainder using diethyl ether followed by drying in the vacuum oven at 50°C overnight. Then, PbI_2 (99.99%; trace metals basis, Acros Organics) and BdAI with a stoichiometric molar ratio of 1:1 were dissolved in a mixture of concentrated hydroiodic acid (57 wt %) and hypophosphorus acid solution (Sigma-Aldrich) with a stoichiometric volume ratio of 1:0.025 using magnetic stirring, which resulted in a solution with a final molar concentration of 0.1 to 0.15 M. The solution was then stirred and heated at ~135°C for 1 hour, which formed a clear yellow solution. The obtained solution was then slowly cooled down to RT at a rate of 5°C/hour. The obtained SCs were then isolated with vacuum filtration thoroughly dried under reduced pressure.

Sample characterization

The RT XRD pattern of 2D perovskite SC flakes was collected using a Bruker-AXS D8 Advance x-ray diffractometer equipped with Cu Kα (λ = 1.5418 Å) x-ray source. The measurement was performed in the 2θ mode between 3° and 50° with a step size of 0.02° and the integration time of 1 s per step. The in situ temperature-dependent XRD pattern of $(PEA)_2PbI_4$ films between 30° and 85°C was measured using a Bruker D8 Discover equipped with Anton Paar DHS1100 vacuum heating chamber and a LYNXEYE detector. The measurement was performed in 2θ mode between 3° and 60° with a step size of 0.02° and integration time of 1 s per step. For each temperature measurement, the sample's temperature was allowed to stabilize with a waiting time of about 20 min. The complex refractive indexes of the samples were measured by using a commercial spectroscopic ellipsometer (J.A. Woolam Company). Variable incidence angle measurements were performed from 65° to 75° with a step size of 5° to obtain accurate fitting parameters. Detailed fitting process refers to (*50*).

TR spectroscopy

TR spectra were collected using an integrated Helios and EOS setup (Ultrafast Systems LLC), which works in a nondegenerate pump-probe configuration. The pump pulses were generated from a Coherent TOPAS-C optical parametric amplifier pumped by a 1-kHz regenerative amplifier (Coherent Legend, 800 nm, 150 fs). The amplifier was seeded by a mode-lock Ti-sapphire oscillator (Coherent Vitesse, 100 fs, 80 MHz). A 400-nm pulse pump was generated by doubling an 800-nm pulse with a beta barium borate crystal. The white light continuum probe pulses were produced by focusing the 800-nm femtosecond pulses through a 2-mm sapphire plate. The probe incidence angle is 13°. A 750-nm short-pass filter was placed before the sample to filter out the 800-nm residue. A reference probe light before the sample and the signal probe light were collected using the same complementary metal-oxide semiconductor sensors.

DFT calculations

For calculations of the crystal structure optimization and DP constants of $(PEA)_2PbI_4$, we used the all-electron-like projector augmented wave method (*51*) and Perdew-Burke-Ernserhof revised for solids exchange correlation potential (*52*), as implemented in the Vienna Ab Initio Simulation Package (VASP) code (*53*). The semicore of Pb atoms (5d orbital) was treated as valence electrons, i.e., 14 valence electrons for Pb ($5d^{10}6s^26p^2$) atom. The cutoff energy for the plane wave expansion of the wave functions is 500 eV. The primitive cell was fully optimized, including its lattice vectors and atomic positions. The Hellman-Feynman forces are less than 1 meV/Å. The spin-orbit coupling effect was taken into consideration because of heavy valence electrons from Pb ions. The 4 × 4 × 1 Monkhorst-Pack grid of *k*-points (*54*) for the Brillouin zone integration of $(PEA)_2PbI_4$ was used in the calculations for structure optimization. The optimized lattice constants are $a = 8.624$ Å, $b = 8.616$ Å, $c = 33.349$ Å, $\alpha = 85.83°$, $\beta = 85.89°$, and $\gamma = 89.50°$. The absolute DP (ADP) is defined as $a^{s}_{V} = V_0 dE^{s}/dV$ for energy state s, where V_0 is the balanced volume of the $(PEA)_2PbI_4$ unit cell. The calculation of DP is based on the methods by Wei and Zunger (*55*). The calculated ADPs for CBM and VBM are −1.29 and −2.60 eV, respectively. The bandgap ADP is defined as $a_V^{gap} = a_V^{CBM} - a_V^{VBM} = 1.31$ eV, and the total ADP is defined as $a_V = a_V^{CBM} + a_V^{VBM} = -3.89$ eV (*19*). We find that both ADPs of VBM and CBM are negative, whereas the bandgap ADP is positive, suggesting that the energy levels exhibit an inverse relationship compared to that of the bandgap under pressure.

SUPPLEMENTARY MATERIALS

Supplementary material for this article is available at https://science.org/doi/10.1126/sciadv.abq1971

REFERENCES AND NOTES

1. J.-C. Blancon, A. V. Stier, H. Tsai, W. Nie, C. C. Stoumpos, B. Traore, L. Pedesseau, M. Kepenekian, F. Katsutani, G. T. Noe, J. Kono, S. Tretiak, S. A. Crooker, C. Katan, M. G. Kanatzidis, J. J. Crochet, J. Even, A. D. Mohite, Scaling law for excitons in 2D perovskite quantum wells. *Nat. Commun.* **9**, 2254 (2018).
2. J. Fu, M. Li, A. Solanki, Q. Xu, Y. Lekina, S. Ramesh, Z. X. Shen, T. C. Sum, Electronic states modulation by coherent optical phonons in 2D halide perovskites. *Adv. Mater.* **33**, 2006233 (2021).
3. D. B. Straus, S. Hurtado Parra, N. Iotov, J. Gebhardt, A. M. Rappe, J. E. Subotnik, J. M. Kikkawa, C. R. Kagan, Direct observation of electron–phonon coupling and slow vibrational relaxation in organic–inorganic hybrid perovskites. *J. Am. Chem. Soc.* **138**, 13798–13801 (2016).
4. T. Ishihara, Optical properties of PbI-based perovskite structures. *JOL* **60-61**, 269–274 (1994).
5. S. Kishimoto, K. Shibuya, F. Nishikido, M. Koshimizu, R. Haruki, Y. Yoda, Subnanosecond time-resolved x-ray measurements using an organic-inorganic perovskite scintillator. *Appl. Phys. Lett.* **93**, 261901 (2008).
6. Z. Wang, Q. Lin, F. P. Chmiel, N. Sakai, L. M. Herz, H. J. Snaith, Efficient ambient-air-stable solar cells with 2D–3D heterostructured butylammonium-caesium-formamidinium lead halide perovskites. *Nat. Energy* **2**, 17135 (2017).
7. C. Qin, T. Matsushima, W. J. Potscavage, A. S. Sandanayaka, M. R. Leyden, F. Bencheikh, K. Goushi, F. Mathevet, B. Heinrich, G. Yumoto, Y. Kanemitsu, C. Adachi, Triplet management for efficient perovskite light-emitting diodes. *Nat. Photon.* **14**, 70–75 (2020).
8. J. Feng, C. Gong, H. Gao, W. Wen, Y. Gong, X. Jiang, B. Zhang, Y. Wu, Y. Wu, H. Fu, L. Jiang, X. Zhang, Single-crystalline layered metal-halide perovskite nanowires for ultrasensitive photodetectors. *Nat. Electron.* **1**, 404–410 (2018).
9. M. A. Haque, S. Kee, D. R. Villalva, W. L. Ong, D. Baran, Halide perovskites: Thermal transport and prospects for thermoelectricity. *Adv. Sci.* **7**, 1903389 (2020).
10. C. Zhu, X. Niu, Y. Fu, N. Li, C. Hu, Y. Chen, X. He, G. Na, P. Liu, H. Zai, Y. Ge, Y. Lu, X. Ke, Y. Bai, S. Yang, P. Chen, Y. Li, M. Sui, L. Zhang, H. Zhou, Q. Chen, Strain engineering in perovskite solar cells and its impacts on carrier dynamics. *Nat. Commun.* **10**, 815 (2019).
11. J. Zhao, Y. Deng, H. Wei, X. Zheng, Z. Yu, Y. Shao, J. E. Shield, J. Huang, Strained hybrid perovskite thin films and their impact on the intrinsic stability of perovskite solar cells. *Sci. Adv.* **3**, eaao5616 (2017).
12. Y. Chen, Y. Lei, Y. Li, Y. Yu, J. Cai, M.-H. Chiu, R. Rao, Y. Gu, C. Wang, W. Choi, H. Hu, C. Wang, Y. Li, J. Song, J. Zhang, B. Qi, M. Lin, Z. Zhang, A. E. Islam, B. Maruyama, S. Dayeh, L.-J. Li, K. Yang, Y.-H. Lo, S. Xu, Strain engineering and epitaxial stabilization of halide perovskites. *Nature* **577**, 209–215 (2020).
13. C.-C. Shen, M.-Y. Weng, J.-K. Sheu, Y.-T. Yao, C.-K. Sun, In situ monitoring of chemical reactions at a solid–water interface by femtosecond acoustics. *J. Phys. Chem. Lett.* **8**, 5430–5437 (2017).
14. A. Scherbakov, P. Van Capel, A. Akimov, J. Dijkhuis, D. Yakovlev, T. Berstermann, M. Bayer, Chirping of an optical transition by an ultrafast acoustic soliton train in a semiconductor quantum well. *Phys. Rev. Lett.* **99**, 057402 (2007).
15. E. S. K. Young, A. V. Akimov, M. Henini, L. Eaves, A. J. Kent, Subterahertz acoustical pumping of electronic charge in a resonant tunneling device. *Phys. Rev. Lett.* **108**, 226601 (2012).
16. O. Kovalenko, T. Pezeril, V. V. Temnov, New concept for magnetization switching by ultrafast acoustic pulses. *Phys. Rev. Lett.* **110**, 266602 (2013).
17. P. Maity, J. Yin, B. Cheng, J.-H. He, O. M. Bakr, O. F. Mohammed, Layer-dependent coherent acoustic phonons in two-dimensional Ruddlesden–Popper perovskite crystals. *J. Phys. Chem. Lett.* **10**, 5259–5264 (2019).
18. P. Guo, C. C. Stoumpos, L. Mao, S. Sadasivam, J. B. Ketterson, P. Darancet, M. G. Kanatzidis, R. D. Schaller, Cross-plane coherent acoustic phonons in two-dimensional organic-inorganic hybrid perovskites. *Nat. Commun.* **9**, 2019 (2018).
19. P.-A. Mante, C. C. Stoumpos, M. G. Kanatzidis, A. Yartsev, Electron–acoustic phonon coupling in single crystal $CH_3NH_3PbI_3$ perovskites revealed by coherent acoustic phonons. *Nat. Commun.* **8**, 14398 (2017).
20. B. Wu, W. Ning, Q. Xu, M. Manjappa, M. Feng, S. Ye, J. Fu, S. Lie, T. Yin, F. Wang, T. W. Goh, P. C. Harikesh, Y. K. E. Tay, Z. X. Shen, F. Huang, R. Singh, G. Zhou, F. Gao, T. C. Sum, Strong self-trapping by deformation potential limits photovoltaic performance in bismuth double perovskite. *Sci. Adv.* **7**, eabd3160 (2021).
21. P. Guo, Y. Xia, J. Gong, C. C. Stoumpos, K. M. McCall, G. C. Alexander, Z. Ma, H. Zhou, D. J. Gosztola, J. B. Ketterson, M. G. Kanatzidis, T. Xu, M. K. Y. Chan, R. D. Schaller, Polar fluctuations in metal halide perovskites uncovered by acoustic phonon anomalies. *ACS Energy Lett.* **2**, 2463–2469 (2017).
22. J. Fu, Q. Xu, G. Han, B. Wu, C. H. A. Huan, M. L. Leek, T. C. Sum, Hot carrier cooling mechanisms in halide perovskites. *Nat. Commun.* **8**, 1300 (2017).
23. M. Li, J. Fu, Q. Xu, T. C. Sum, Slow hot-carrier cooling in halide perovskites: Prospects for hot-carrier solar cells. *Adv. Mater.* **31**, 1802486 (2019).
24. C. Thomsen, H. T. Grahn, H. J. Maris, J. Tauc, Surface generation and detection of phonons by picosecond light pulses. *Phys. Rev. B* **34**, 4129–4138 (1986).
25. Y. Yang, Y. Yan, M. Yang, S. Choi, K. Zhu, J. M. Luther, M. C. Beard, Low surface recombination velocity in solution-grown $CH_3NH_3PbBr_3$ perovskite single crystal. *Nat. Commun.* **6**, 7961 (2015).
26. P. Ruello, V. E. Gusev, Physical mechanisms of coherent acoustic phonons generation by ultrafast laser action. *Ultrasonics* **56**, 21–35 (2015).
27. Y. Zhai, S. Baniya, C. Zhang, J. Li, P. Haney, C.-X. Sheng, E. Ehrenfreund, Z. V. Vardeny, Giant Rashba splitting in 2D organic-inorganic halide perovskites measured by transient spectroscopies. *Sci. Adv.* **3**, e1700704 (2017).
28. C.-K. Sun, J.-C. Liang, X.-Y. Yu, Coherent acoustic phonon oscillations in semiconductor multiple quantum wells with piezoelectric fields. *Phys. Rev. Lett.* **84**, 179–182 (2000).
29. K.-z. Du, Q. Tu, X. Zhang, Q. Han, J. Liu, S. Zauscher, D. B. Mitzi, Two-dimensional lead (II) halide-based hybrid perovskites templated by acene alkylamines: Crystal structures, optical properties, and piezoelectricity. *Inorg. Chem.* **56**, 9291–9302 (2017).
30. W. Peng, J. Yin, K.-T. Ho, O. Ouellette, M. De Bastiani, B. Murali, O. El Tall, C. Shen, X. Miao, J. Pan, E. Alarousu, J.-H. He, B. S. Ooi, O. F. Mohammed, E. Sargent, O. M. Bakr, Ultralow self-doping in two-dimensional hybrid perovskite single crystals. *Nano Lett.* **17**, 4759–4767 (2017).
31. P. Ruello, S. Zhang, P. Laffez, B. Perrin, V. Gusev, Laser-induced coherent acoustical phonons mechanisms in the metal-insulator transition compound $NdNiO_3$: Thermal and nonthermal processes. *Phys. Rev. B* **79**, 094303 (2009).
32. M. A. Reyes-Martinez, P. Tan, A. Kakekhani, S. Banerjee, A. A. Zhumekenov, W. Peng, O. M. Bakr, A. M. Rappe, Y.-L. Loo, Unraveling the elastic properties of (quasi) two-dimensional hybrid perovskites: A joint experimental and theoretical study. *ACS Appl. Mater. Interfaces* **12**, 17881–17892 (2020).

33. A. Giri, A. Z. Chen, A. Mattoni, K. Aryana, D. Zhang, X. Hu, S.-H. Lee, J. J. Choi, P. E. Hopkins, Ultralow thermal conductivity of two-dimensional metal halide perovskites. *Nano Lett.* **20**, 3331–3337 (2020).
34. Y.-H. Li, X. G. Gong, S.-H. Wei, Ab initio all-electron calculation of absolute volume deformation potentials of IV-IV, III-V, and II-VI semiconductors: The chemical trends. *Phys. Rev. B* **73**, 245206 (2006).
35. D. Wang, B. Wen, Y.-N. Zhu, C.-J. Tong, Z.-K. Tang, L.-M. Liu, First-principles study of novel two-dimensional $(C_4H_9NH_3)_2PbX_4$ perovskites for solar cell absorbers. *J. Phys. Chem. Lett.* **8**, 876–883 (2017).
36. W.-J. Yin, T. Shi, Y. Yan, Unusual defect physics in $CH_3NH_3PbI_3$ perovskite solar cell absorber. *Appl. Phys. Lett.* **104**, 063903 (2014).
37. V. A. Hintermayr, L. Polavarapu, A. S. Urban, J. Feldmann, Accelerated carrier relaxation through reduced coulomb screening in two-dimensional halide perovskite nanoplatelets. *ACS Nano* **12**, 10151–10158 (2018).
38. O. Wright, V. Gusev, Acoustic generation in crystalline silicon with femtosecond optical pulses. *Appl. Phys. Lett.* **66**, 1190–1192 (1995).
39. B. Guzelturk, T. Winkler, T. W. Van de Goor, M. D. Smith, S. A. Bourelle, S. Feldmann, M. Trigo, S. W. Teitelbaum, H.-G. Steinrück, G. A. de la Pena, R. Alonso-Mori, D. Zhu, T. Sato, H. I. Karunadasa, M. F. Toney, F. Deschler, A. M. Lindenberg, Visualization of dynamic polaronic strain fields in hybrid lead halide perovskites. *Nat. Mater.* **20**, 618–623 (2021).
40. M. Li, S. Bhaumik, T. W. Goh, M. S. Kumar, N. Yantara, M. Grätzel, S. Mhaisalkar, N. Mathews, T. C. Sum, Slow cooling and highly efficient extraction of hot carriers in colloidal perovskite nanocrystals. *Nat. Commun.* **8**, 14350 (2017).
41. A. Lemmerer, D. G. Billing, Lead halide inorganic–organic hybrids incorporating diammonium cations. *CrstEngComm* **14**, 1954–1966 (2012).
42. F. Vialla, N. D. Fatti, Time-domain investigations of coherent phonons in van der waals thin films. *Nanomaterials* **10**, 2543 (2020).
43. Y. Gao, S. Kim, S. Zhou, H.-C. Chiu, D. Nélias, C. Berger, W. De Heer, L. Polloni, R. Sordan, A. Bongiorno, E. Riedo, Elastic coupling between layers in two-dimensional materials. *Nat. Mater.* **14**, 714–720 (2015).
44. T. Zhu, E. Ertekin, Mixed phononic and non-phononic transport in hybrid lead halide perovskites: Glass-crystal duality, dynamical disorder, and anharmonicity. *Energ. Environ. Sci.* **12**, 216–229 (2019).
45. F. Krasniqi, S. Johnson, P. Beaud, M. Kaiser, D. Grolimund, G. Ingold, Influence of lattice heating time on femtosecond laser-induced strain waves in InSb. *Phys. Rev. B* **78**, 174302 (2008).
46. W. Thurber, A. Mante, Thermal conductivity and thermoelectric power of rutile (TiO_2). *Phys. Rev.* **139**, A1655–A1665 (1965).
47. B. Li, Y. Kawakita, Y. Liu, M. Wang, M. Matsuura, K. Shibata, S. Ohira-Kawamura, T. Yamada, S. Lin, K. Nakajima, S. Liu, Polar rotor scattering as atomic-level origin of low mobility and thermal conductivity of perovskite $CH_3NH_3PbI_3$. *Nat. Commun.* **8**, 16086 (2017).
48. C. C. Stoumpos, D. H. Cao, D. J. Clark, J. Young, J. M. Rondinelli, J. I. Jang, J. T. Hupp, M. G. Kanatzidis, Ruddlesden–Popper hybrid lead iodide perovskite 2D homologous semiconductors. *Chem. Mater.* **28**, 2852–2867 (2016).
49. I.-H. Park, Q. Zhang, K. C. Kwon, Z. Zhu, W. Yu, K. Leng, D. Giovanni, H. S. Choi, I. Abdelwahab, Q.-H. Xu, T. C. Sum, K. P. Loh, Ferroelectricity and Rashba effect in a two-dimensional Dion-Jacobson hybrid organic–inorganic perovskite. *J. Am. Chem. Soc.* **141**, 15972–15976 (2019).
50. B. Song, J. Hou, H. Wang, S. Sidhik, J. Miao, H. Gu, H. Zhang, S. Liu, Z. Fakhraai, J. Even, J.-C. Blancon, A. D. Mohite, D. Jariwala, Determination of dielectric functions and exciton oscillator strength of two-dimensional hybrid perovskites. *ACS Mater. Lett.* **3**, 148–159 (2020).
51. P. E. Blöchl, Projector augmented-wave method. *Phys. Rev. B* **50**, 17953–17979 (1994).
52. J. P. Perdew, A. Ruzsinszky, G. I. Csonka, O. A. Vydrov, G. E. Scuseria, L. A. Constantin, X. Zhou, K. Burke, Restoring the density-gradient expansion for exchange in solids and surfaces. *Phys. Rev. Lett.* **100**, 136406 (2008).
53. G. Kresse, J. Furthmüller, Efficient iterative schemes for ab initio total-energy calculations using a plane-wave basis set. *Phys. Rev. B* **54**, 11169–11186 (1996).
54. H. J. Monkhorst, J. D. Pack, Special points for Brillouin-zone integrations. *Phys. Rev. B* **13**, 5188–5192 (1976).
55. S.-H. Wei, A. Zunger, Predicted band-gap pressure coefficients of all diamond and zinc-blende semiconductors: Chemical trends. *Phys. Rev. B* **60**, 5404–5411 (1999).
56. S. A. Akhmanov, V. É. Gusev, Laser excitation of ultrashort acoustic pulses: New possibilities in solid-state spectroscopy, diagnostics of fast processes, and nonlinear acoustics. *Sov. Phys. Uspekhi* **35**, 153–191 (1992).
57. L. Bergman, D. Alexson, P. L. Murphy, R. J. Nemanich, M. Dutta, M. A. Stroscio, C. Balkas, H. Shin, R. F. Davis, Raman analysis of phonon lifetimes in AlN and GaN of wurtzite structure. *Phys. Rev. B* **59**, 12977–12982 (1999).
58. V. A. Dragomir, S. Neutzner, C. Quarti, D. Cortecchia, A. Petrozza, S. Roorda, D. Beljonne, R. Leonelli, A. R. S. Kandada, C. Silva, Lattice vibrations and dynamic disorder in two-dimensional hybrid lead-halide perovskites. arXiv:1812.05255 [cond-mat.mtrl-sci] (13 December 2018).
59. K. Ishioka, A. Rustagi, U. Höfer, H. Petek, C. J. Stanton, Intrinsic coherent acoustic phonons in the indirect band gap semiconductors Si and GaP. *Phys. Rev. B* **95**, 035205 (2017).
60. D. H. Hurley, O. B. Wright, Detection of ultrafast phenomena by use of a modified Sagnac interferometer. *Opt. Lett.* **24**, 1305–1307 (1999).
61. S. Neutzner, F. Thouin, D. Cortecchia, A. Petrozza, C. Silva, A. R. S. Kandada, Exciton-polaron spectral structures in two-dimensional hybrid lead-halide perovskites. *Phys. Rev. Mater.* **2**, 064605 (2018).
62. M. Safdari, P. H. Svensson, M. T. Hoang, I. Oh, L. Kloo, J. M. Gardner, Layered 2D alkyldiammonium lead iodide perovskites: Synthesis, characterization, and use in solar cells. *J. Mater. Chem. A* **4**, 15638–15646 (2016).

Acknowledgments: The computational work for this article was (fully/partially) performed on resources of the National Supercomputing Centre (NSCC), Singapore (https://www.nscc.sg). **Funding:** This research/project was supported by the Ministry of Education under its AcRF Tier 2 grants (MOE2019-T2-1-006, MOE-T2EP20120-0013, and MOE-T2EP50120-0004) and the National Research Foundation (NRF) Singapore under its NRF Investigatorship (NRF-NRFI-2018-04). K.P.L. acknowledges support from the Ministry of Education (MOE) Singapore under AcRF Tier 2 grant (MOE2019-T2-1-037). N.M. and B.F. acknowledge support from the Singapore National Research Foundation through the Intra-CREATE Collaborative Grant (NRF2018-ITC001-001). H.S. and T.Y. acknowledge support from the Singapore National Research Foundation via Competitive Research Programmes (NRF-CRP21-2018-0007 and NRF-CRP23-2019-0007). **Author contributions:** T.C.S. and J.F. conceived the idea for the manuscript and designed the experiments. J.F. conducted the spectroscopic characterization. Q.X. conducted the DFT calculations. I.A., R.C., B.F., and T.Y. prepared the samples and performed the XRD and ellipsometry measurement. J.F. and T.C.S. analyzed the data and wrote the manuscript. All authors discussed the results and commented on the manuscript at all stages. T.C.S. led the project. **Competing interests:** The authors declare that they have no competing interests. **Data and materials availability:** All data needed to evaluate the conclusions in the paper are present in the paper and/or the Supplementary Materials. The data that support the findings of this study are openly available in DR-NTU (Data) at https://doi.org/10.21979/N9/5BKLHK.

Submitted 24 March 2022
Accepted 1 August 2022
Published 16 September 2022
10.1126/sciadv.abq1971